



HAL
open science

A Novel Survey for Young Substellar Objects with the W-band Filter. V. IC 348 and Barnard 5 in the Perseus Cloud

Bhavana Lalchand, Wen-Ping Chen, Beth A. Biller, Loïc Albert, Katelyn Allers, Sophie Dubber, Zhoujian Zhang, Michael C. Liu, Jessy Jose, Belinda Damian, et al.

► **To cite this version:**

Bhavana Lalchand, Wen-Ping Chen, Beth A. Biller, Loïc Albert, Katelyn Allers, et al.. A Novel Survey for Young Substellar Objects with the W-band Filter. V. IC 348 and Barnard 5 in the Perseus Cloud. *The Astronomical Journal*, 2022, 164, 10.3847/1538-3881/ac8547 . insu-03860282

HAL Id: insu-03860282

<https://insu.hal.science/insu-03860282>

Submitted on 19 Nov 2022

HAL is a multi-disciplinary open access archive for the deposit and dissemination of scientific research documents, whether they are published or not. The documents may come from teaching and research institutions in France or abroad, or from public or private research centers.

L'archive ouverte pluridisciplinaire **HAL**, est destinée au dépôt et à la diffusion de documents scientifiques de niveau recherche, publiés ou non, émanant des établissements d'enseignement et de recherche français ou étrangers, des laboratoires publics ou privés.



Distributed under a Creative Commons Attribution 4.0 International License



A Novel Survey for Young Substellar Objects with the W-band Filter. V. IC 348 and Barnard 5 in the Perseus Cloud

Bhavana Lalchand¹ , Wen-Ping Chen^{1,2} , Beth A. Biller^{3,4} , Loïc Albert⁵, Katelyn Allers⁶, Sophie Dubber^{3,4} , Zhoujian Zhang⁷ , Michael C. Liu⁸ , Jessy Jose⁹ , Belinda Damian¹⁰, Tanvi Sharma¹ , Mickaël Bonnefoy¹¹ , and Yumiko Oasa¹²

¹ Institute of Astronomy, National Central University, 300 Zhongda Road, Zhongli, Taoyuan 32001, Taiwan

² Department of Physics, National Central University, 300 Zhongda Road, Zhongli, Taoyuan 32001, Taiwan

³ SUPA, Institute for Astronomy, University of Edinburgh, Blackford Hill, Edinburgh EH9 3HJ, UK

⁴ Centre for Exoplanet Science, University of Edinburgh, Edinburgh, UK

⁵ Institut de Recherche sur les Exoplanètes (iREx), Université de Montréal, Département de Physique, C.P. 6128 Succ. Centre-ville, Montréal, QC H3C 3J7, Canada

⁶ Department of Physics and Astronomy, Bucknell University, Lewisburg, PA 17837, USA

⁷ The University of Texas at Austin, Department of Astronomy, 2515 Speedway, C1400, Austin, TX 78712, USA

⁸ Institute for Astronomy, University of Hawai'i, 2680 Woodlawn Drive, Honolulu, HI 96822, USA

⁹ Indian Institute of Science Education and Research (IISER) Tirupati, Rami Reddy Nagar, Karakambadi Road, Mangalam (P.O.), Tirupati 517 507, India

¹⁰ CHRIST (Deemed to be University), Hosur Road, Bengaluru 560029, India

¹¹ Univ. Grenoble Alpes, CNRS, IPAG, F-38000 Grenoble, France

¹² Faculty of Education, Graduate School of Science and Engineering, Saitama University, 255 Shimo-Okubo, Sakura-ku, Saitama, 338-8570, Japan

Received 2022 June 6; revised 2022 July 22; accepted 2022 July 27; published 2022 September 6

Abstract

We report the discovery of substellar objects in the young star cluster IC 348 and the neighboring Barnard 5 dark cloud, both at the eastern end of the Perseus star-forming complex. The substellar candidates are selected using narrowband imaging, i.e., on and off photometric technique with a filter centered around the water absorption feature at $1.45\ \mu\text{m}$, a technique proven to be efficient in detecting water-bearing substellar objects. Our spectroscopic observations confirm three brown dwarfs in IC 348. In addition, the source WBIS 03492858+3258064, reported in this work, is the first confirmed brown dwarf discovered toward Barnard 5. Together with the young stellar population selected via near- and mid-infrared colors using the Two Micron All Sky Survey and the Wide-field Infrared Survey Explorer, we diagnose the relation between stellar versus substellar objects with the associated molecular clouds. Analyzed by Gaia EDR3 parallaxes and kinematics of the cloud members across the Perseus region, we propose the star formation scenario of the complex under influence of the nearby OB association.

Unified Astronomy Thesaurus concepts: [Open star clusters \(1160\)](#); [Brown dwarfs \(185\)](#); [Star forming regions \(1565\)](#); [Young stellar objects \(1834\)](#)

1. Introduction

Stars are formed in groups out of dense molecular fragments, whereas planets are condensed in young circumstellar disks. Brown dwarfs (mass $\lesssim 0.07 M_{\odot}$; Dupuy & Liu 2017) and planet-mass objects (mass $\lesssim 0.013 M_{\odot}$), collectively called substellar objects, are not massive enough to sustain core hydrogen fusion and therefore cool and fade after birth, even though massive brown dwarfs are expected to undertake core fusion by short-supplied deuterium and lithium, or even by protons before the core becomes degenerate (e.g., Rebolo et al. 1996; Forbes & Loeb 2019). Young substellar objects are hot and bright and therefore detectable in nearby star-forming regions. For example, a $5 M_{J_{\text{up}}}$ planet is expected to have $T_{\text{eff}} \sim 1800$ K and $\log L/L_{\odot} \sim -3.5$ at an age of 1 Myr, becomes $T_{\text{eff}} \sim 1100$ K and $\log L/L_{\odot} \sim -4.4$ at an age of 10 Myr, and continues to fade to $T_{\text{eff}} \sim 600$ K and $\log L/L_{\odot} \sim -5.7$ at an age of 0.1 Gyr (Burrows et al. 1997), corresponding to absolute J magnitude of $M_J \sim 11$ mag (1 Myr), $M_J \sim 14$ mag (10 Myr), and $M_J \sim 17$ mag (0.1 Gyr), respectively (Allard et al. 2001; Baraffe et al. 2003). This means that such an

object at an age of 1 Myr would have an apparent magnitude of $m_J \sim 18$ mag at 200 pc given a moderate extinction $A_J = 1$ mag.

A reliable catalog of substellar members is the first crucial step to supplement the stellar population within the same cloud, i.e., to derive the mass function, and to test theories of stellar versus substellar formation. At the lowest-mass end, the free-floating planets serve as a comparison sample to exoplanets, as to the similarities and differences in formation and evolution (Lucas & Roche 2000), e.g., to test the progression of cloud fragmentation to very low masses or the existence of a population of ejected giant planets (Sumi et al. 2011).

Wide-field surveys have played a major role in recognition of substellar objects in the solar neighborhood, such as by Pan-STARRS (PS1; Chambers et al. 2016), the Wide-field Infrared Survey Explorer (WISE; Wright et al. 2010), the UKIRT Infrared Deep Sky Survey (UKIDSS; Lawrence et al. 2007), the Two Micron All Sky Survey (2MASS; Skrutskie et al. 2006), the DEep Near-Infrared Survey of the Southern sky (DENIS; Epchtein et al. 1994), the Sloan Digital Sky Survey (SDSS; Blanton et al. 2017), the VISTA Hemisphere Survey (VHS; McMahon et al. 2013), etc. Interstellar dust extinction makes it difficult in optical and near-infrared wavelengths to distinguish between background giant stars and equally faint substellar objects. The largest limiting factor for these surveys is the need for spectroscopic confirmation of photometrically selected candidates, which is very time-consuming unless a



Original content from this work may be used under the terms of the [Creative Commons Attribution 4.0 licence](#). Any further distribution of this work must maintain attribution to the author(s) and the title of the work, journal citation and DOI.

highly reliable candidate list is available. Supplementing the usual broadband photometry to diagnose cool atmospheres, we use a custom IR filter (with a bandpass width 6%) centered around $1.45\ \mu\text{m}$ to detect the flux suppression due to H_2O absorption commonly seen in the spectra of low-mass stars, brown dwarfs, and planetary-mass objects (Allers & Liu 2020). The combination of the water band (referred to as the W band) photometry along with J and H magnitudes proves effective in distinguishing young substellar objects from reddened background stars that lack water absorption in their atmospheres (Jose et al. 2020; Dubber et al. 2021).

The Perseus molecular cloud complex, located to the west of the Per OB2 association, is active in star formation, with a few distinct subregions, including two young populous star clusters, IC 348 and NGC 1333, and dark clouds such as L1468, L1448, L1451, L1455, Barnard 1, and Barnard 5 (B5, also known as L1471; Jørgensen et al. 2006; Rebull et al. 2007). Here we report identification of substellar objects in IC 348 and in B5, both to the eastern end of the complex. This list, together with the young stellar counterparts, provides two contrasting samples, a crowded (IC 348) versus a relatively isolated (B5) environment.

IC 348 ($\alpha = 03^{\text{h}}44^{\text{m}}30^{\text{s}}.78$, $\delta = +32^{\circ}10'19''0$, J2000) harbors nearly 500 known members (Luhman et al. 2016), with the most massive being a B5 star (HD 281159). Distance determinations to the cluster range from $321 \pm 10\ \text{pc}$ by Ortiz-León et al. (2018) using VLBA, to $320 \pm 26\ \text{pc}$ by Gaia Collaboration et al. (2016, 2018), to $295 \pm 15\ \text{pc}$ by Zucker et al. (2018). The age of the cluster has been estimated to be 2–3 Myr (Luhman et al. 2003). However, the young population seems to have a lower disk fraction given its age (Cieza et al. 2015). Indeed, Ruíz-Rodríguez et al. (2018), using ALMA, detected typical disk masses in the Class II objects in IC 348 to be lower than in Taurus, Chamaeleon, or σOri , all with ages 1–5 Myr, thus indicating an older age (6 Myr) for IC 348 (Bell et al. 2013; Cottaar et al. 2014). In a separate site $\sim 10'$ to the southwest of the star cluster, ongoing star formation (1–2 Myr) is witnessed to be spatially coincident with dense clouds, protostars, and Herbig-Haro objects, suggestive of noncoeval episodes of star birth in the region (Tafalla et al. 2006).

Farther to the northeast of IC 348 ($\sim 3\ \text{pc}$), at the far end of the cloud complex, is B5, an isolated globule with cold (Beichman et al. 1984) and large dust grains (Bhatt 1986). More distant than IC 348 (350 pc; Herbig & Jones 1983; Langer et al. 1989), and spanning some $45'$ in the sky, B5 is relatively massive ($\sim 10^3 M_{\odot}$; Goldsmith et al. 1986; Langer et al. 1989), and known also to have ongoing star formation, yet hosting several dense cores (Fuller et al. 1991; Hatchell et al. 2005; Olmi et al. 2005; Kirk et al. 2006), fragmenting cloud filaments (Pineda et al. 2015), and Herbig-Haro objects (Walawender et al. 2005). An overall low star formation efficiency is in vast contrast to the adjacent IC 348 cluster, which is prolific in star birth (Hatchell et al. 2007).

This paper is a continuation of the W -band series on substellar objects using the novel W -band technique in nearby star-forming regions (Allers & Liu 2020; Jose et al. 2020; Dubber et al. 2021, Dubber et al. 2022, submitted). We report here deep imaging surveys using the W band, combined with J and H bands, to identify young brown dwarfs in IC 348 and B5. While the young stellar population in IC 348 is relatively well known, our focus in this cloud is on newly found brown dwarfs. For B5, on the other hand, in addition to the substellar candidates found with the W -band imaging, we have conducted

a census of young stars with near- and mid-infrared colors. Finally, we have characterized the distance and kinematics of the young objects found in IC 348 and will discuss them in the context of the overall morphology and motion of the whole Perseus cloud complex as evidence of the star formation history therein.

2. Observation and Data Analysis

The data used in this study include the water-band images to select substellar candidates, plus archival near- and mid-infrared photometry from 2MASS and WISE to identify young stars with dusty circumstellar disks and Gaia EDR3 for parallax and kinematics. The field of view of our water-band images, plus the archival data used is shown in Figure 1.

2.1. CFHT/WIRCam Water-band Imaging

IC 348 was observed on 2016 March 18, 2016 July 16, and 2017 December 8 and B5 was observed on 2015 October 23 (all in UT) with the Canada–France–Hawaii Telescope (CFHT) using the Wide Field Infrared Camera (WIRCam; Puget et al. 2004). With a field of view of $\sim 20' \times 20'$ and ~ 0.306 pixels, we used a 21-point dithering pattern to fill the gaps between the four detectors of WIRCam and to subtract the sky background. Images were processed by the CFHT ‘I’iwi pipeline. Dark exposure times were 10 s in J band and 65 s for H and W bands. Normalized flat-field corrections for each filter were constructed after each observing run. Before stacking the images, saturated and bad pixels were flagged, nonlinearity was corrected, and images were dark subtracted, flat-field corrected, sky subtracted, crosstalk removed and $1/f$ noise corrected by ‘I’iwi. The total integration time for J , H , and W bands for IC 348 was 170, 210, and 1495 s, respectively, and for B5 it was 50 s (J), 75 s (H), and 455 s (W), respectively.

To calibrate the J -band and H -band stacks, we adjusted the zero-point by including a color term between 2MASS and the MKO system of WIRCam by clipping the magnitudes in the ranges $14.5\ \text{mag} \leq J \leq 16\ \text{mag}$ and $14.5\ \text{mag} \leq H \leq 15.5\ \text{mag}$, with the lower limit being the saturation limit of the WIRCam, and the upper limit being decided by the errors of 2MASS magnitudes (i.e., $< 0.1\ \text{mag}$). We used the color correction from Leggett et al. (2006) to convert the 2MASS J and H magnitudes to the MKO system, and then found the zero-point offset for each of the J and H bands.

In the absence of 2MASS equivalents, the zero-point of the W -band photometry was determined with a different strategy. Following Allers & Liu (2020), we adopt a Q index as a measure of the flux suppression in the W band relative to the dereddened continuum between J and H bands, as shown in the following equation:

$$Q = (J - W) + e(H - W), \quad (1)$$

where J and H are the magnitudes already calibrated, W is the W -band magnitude to be calibrated, and $e = (A_J - A_W)/(A_W - A_H)$ is an empirical coefficient to account for the reddening across the bands. To calibrate the W magnitude, the median Q value, Q_f , for the majority of bright stars most likely lacking water absorption is adjusted so that $Q_f \approx 0$, that is,

$$W = (eH + J - Q_f)/(1.0 + e), \quad (2)$$

which is based on our synthetic photometry for a field star (i.e., M0), yielding $Q_f = -0.043$, and we have adopted $e = 1.61$ (Allers & Liu 2020). The W -band zero-point is then applied to

offset the WIRCam instrumental magnitude. The calibrated J , H , and W magnitudes together allow the Q index to be used to quantify the flux suppression in the W band to select water-bearing candidates, with the methodology to be detailed later in Section 3.1.

2.2. Spectroscopic Observations

Spectroscopic follow-up observations were conducted with the SpeX spectrograph on the Infrared Telescope Facility (IRTF; Rayner et al. 2003). The targets were chosen as being sufficiently bright ($H < 17$ mag) and were checked as to whether they were already known brown dwarfs (Muench et al. 2007; Alves de Oliveira et al. 2013; Luhman et al. 2016). We incorporated available information from SIMBAD, 2MASS, Pan-STARRS, and UKIDSS photometry. The targets were selected for spectroscopic follow up with no photometric peculiarity.

Three targets in IC 348 were observed on 2017 February 18, and one target on 2022 January 12 (all in UT). A standard ABBA nodding pattern was utilized to obtain the sky and target data, with a total integration time of 1473 s for each target. The observations were taken in the prism mode using a $0''.8$ slit, which corresponds to an average resolving power of $R \sim 100$. Flat-field frames and wavelength calibration using an argon lamp were taken before or after a set of observations. We used SPEXTOOL (V4.1; Cushing et al. 2005), an IDL-based data reduction package, to extract the spectra. An A0 standard star, either HD 25152 or HD 23512, was observed either before or after a science target for telluric corrections. The IRTF spectra for IC 348 are shown in Figure 2.

Three B5 targets were observed on 2022 January 12 (UT), also in the prism mode, but with a $0''.5$ slit and with the standard star HD 22859, following the same data reduction procedure. The spectra of the three B5 targets are shown in Figure 3.

2.3. WISE and 2MASS

The census of the young stellar population in IC 348 has been relatively comprehensive in the literature; therefore, our attention was mainly on the substellar objects, but for B5 we pay attention to the stellar and substellar objects in general. We conducted a search within a field of $\sim 30'$ toward B5 for young stellar candidates using near- and mid-infrared colors, with 2MASS (Cutri et al. 2003) photometry in J ($1.25 \mu\text{m}$), H ($1.65 \mu\text{m}$), and K_s ($2.15 \mu\text{m}$), and WISE (Cutri et al. 2012) in W1 ($3.4 \mu\text{m}$), W2 ($4.6 \mu\text{m}$), W3 ($12 \mu\text{m}$), and W4 ($22 \mu\text{m}$) bands. There are 10,588 WISE sources within the B5 field, of which 1140 have photometric quality flag “AAA” (206) or “AAB” (934), i.e., with an uncertainty less than 0.1 mag (for A) or 0.3 mag (for B) in respective bands, whereas among the 4282 2MASS sources, 1985 have photometric quality flag “AAA” with uncertainty $\lesssim 0.1$ mag.

2.4. Gaia EDR3

We made use of the Gaia Early Data Release 3 (Gaia EDR3; Gaia Collaboration et al. 2021), which provides homogeneous astrometry (coordinates, trigonometric parallax, and proper motion) of about 1.5 billion sources of the entire sky. Broadband photometries in G , G_{BP} , and G_{RP} with passbands of 330–1050 nm, 330–680 nm, and 630–1050 nm, respectively, are also available. We analyzed the Gaia EDR3 data toward

IC 348, B5, and three other regions in the Perseus complex to diagnose the parallax and kinematic properties.

3. Young Stellar and Substellar Members

3.1. Selection of Brown Dwarf Candidates

The use of the Q index (Equation (1)) to distinguish brown dwarfs from reddened background objects (see Allers & Liu 2020; Jose et al. 2020; Dubber et al. 2021, for detailed descriptions) is much more effective than using broadband photometric colors alone. The reddening-insensitive index is constructed using Equation (1) and the extinction ratio $e = (A_J - A_W)/(A_W - A_H)$ in the three bands J , H , W . To set this value, we calculated synthetic photometry for M0 spectra taken from Kirkpatrick et al. (2010), reddened by the $A_V = 10$ mag and $R_V = 3.1$ reddening law of Fitzpatrick (1999). Next, we compared the reddened and unreddened synthetic photometry of the M0 spectra and adopted an extinction coefficient of $e = 1.61$ (see Allers & Liu 2020). A typical contaminant star would have $Q \sim 0$ (without water absorption), whereas for a later-type object the Q index would be negative owing to water absorption, as presented in Figure 4 for IC 348. By using the synthetic photometry in J , H , and W of young objects (Muench et al. 2007; Allers & Liu 2013) and field dwarfs (Cushing et al. 2005), we concluded that objects with spectral types later than M6 would have $Q < -0.6$. Including the uncertainty σ_Q , estimated by calculating the errors in quadrature, namely,

$$\sigma_Q = \sqrt{\sigma_J^2 + (e \sigma_H)^2 + [(1 + e) \sigma_W]^2}, \quad (3)$$

we therefore considered sources with $Q \leq -(0.6 + \sigma_Q)$ for the plausible presence of water absorption, i.e., as substellar candidates, and with $H > 14$ mag to avoid photometric saturation. The limitation to our approach is that if a young substellar object is still embedded in the parental material and/or has a substantial mass accretion, thereby entailing strong veiling (Luhman & Rieke 1999), our technique may not be able to identify it. In addition to molecular features, criteria of cool atmospheres can be added (e.g., Chiang et al. 2015). For this we imposed the condition $(W1-W2) > 0.10$, the intrinsic color for a spectral type later than M6 (Kirkpatrick et al. 2011). We also cross-matched with Pan-STARRS 1 (Chambers et al. 2016) to remove objects with bright optical counterparts, i.e., $(z_{PS1} - J_{CFHT}) \leq 2$ (Knapp et al. 2004). Given the spatial resolutions of WISE ($\sim 6''$), CFHT ($\sim 0.306''$), and Pan-STARRS1 ($\sim 0.258''$); images of all candidates were inspected by eye to ensure that the $(W1-W2)$ color was not affected by blends with other sources. Combining both the water absorption and cool temperature criteria, i.e., $(W1-W2) > 0.10$ and $(z_{PS1} - J_{CFHT}) \leq 2$, and by excluding any known members found in the literature (i.e., Muench et al. 2007; Alves de Oliveira et al. 2013; Luhman et al. 2016), we obtained a final list of four targets in IC 348 and three targets in B5, shown in Figures 4 and 6, for follow-up spectroscopy. In Figure 5 we demonstrate that an increasingly negative value of Q corresponds to an object with a later type. Here we show Q versus spectral type (SpT) of all the known members in the

Table 1
Properties of Newly Identified Substellar Objects in IC 348 and Barnard 5

ID WBIS	α (J2000) (deg)	δ (J2000) (deg)	J (mag)	H (mag)	W1–W2 (mag)	$z_{\text{PS1}} - J_{\text{CFHT}}$ (mag)	Q	SpT ^a	A_V (mag)	Age ^b	$\log(L_{\text{bol}}/L_{\odot})$	T_{eff} (10^3 K)
IC 348												
03435016+3204073 ^c	55.95905	+32.06875	17.64 ± 0.03	15.33 ± 0.01	0.59	...	-0.65 ± 0.05	M5.5	18.79	VL-G	$-0.65_{-0.135}^{+0.129}$	2.92 ± 22
03441864+3218204	56.07767	+32.30568	15.79 ± 0.01	15.16 ± 0.01	0.19	1.99	-0.74 ± 0.04	M6	0.40	INT-G (I)	$-2.25_{-0.117}^{+0.094}$	2.86 ± 38
03451508+3218215	56.31284	+32.30598	13.32 ± 0.01	12.38 ± 0.01	0.28	3.04	-0.66 ± 0.03	M5	4.62	INT-G (I)	$-1.54_{0.097}^{+0.089}$	3.09 ± 49
Barnard 5												
↖ 03492858+3258064	57.36907	+32.96845	14.77 ± 0.01	14.12 ± 0.01	0.29	2.29	-0.75 ± 0.03	M6	1.21	INT-G (I)	$-1.95_{0.111}^{+0.076}$	2.86 ± 9

Notes.

^a The uncertainty in the spectral classification type is 0.5 subtype.

^b The age is estimated based on spectral fitting in Dubber et al. (2021; please see Figure 7).

^c This target does not have a counterpart in the Pan-STARRS (PS1) catalog. The PS1 images were visually inspected. The target is not visible in g , r , or i band and is faint in z and y bands.

Table 2
Contaminants with Spectroscopic Follow Up and the Remaining Candidate Substellar Objects in IC 348 and Barnard 5

ID WBIS	RA (J2000) (deg)	DEC (J2000) (deg)	J (mag)	H (mag)	W1–W2 (mag)	$z_{\text{PS1}} - J_{\text{CFHT}}$ (mag)	Q	SpT _a	A_V (mag)	Age	$\log(L_{\text{bol}}/L_{\odot})$	T_{eff} (10^3 K)
IC 348												
03434538+3201041	55.93912	+32.01781	16.69 ± 0.02	14.92 ± 0.01	0.315	3.52	-0.79 ± 0.04	<M4	13.07	...	$-0.91_{-0.156}^{-0.129}$	3.81 ± 83
Barnard 5												
03481542+3309185	57.06426	+33.15515	14.83 ± 0.01	14.08 ± 0.01	0.19	1.68	-0.71 ± 0.02	M4	0.85	FLD-G	$-1.99_{0.108}^{0.079}$	3.09 ± 53
03483616+3259054	57.15066	+32.98484	16.78 ± 0.04	15.86 ± 0.03	0.10	2.45	-0.71 ± 0.10	<M4	2.56	INT-G (Y)	$-1.73_{0.112}^{0.077}$	3.30 ± 125
03482654+3252117	57.11059	+32.86992	19.31 ± 0.08	18.32 ± 0.06	0.11	2.83	-0.92 ± 0.22	BDc
03475398+3253030	56.97494	+32.88416	17.44 ± 0.03	17.35 ± 0.03	0.12	5.99	-0.82 ± 0.11	BDc
03484769+3301185	57.19872	+33.02181	18.65 ± 0.08	17.83 ± 0.06	0.12	4.32	-0.83 ± 0.22	BDc

Note. The uncertainty in the spectral classification type is 0.5 subtype. BDc refers to brown dwarf candidate.

Table 3
Young Stellar Objects Identified in Barnard 5 Using WISE and 2MASS

ID	α_{J2000} (deg)	δ_{J2000} (deg)	W1 (mag)	W2 (mag)	W3 (mag)	<i>J</i> (mag)	<i>H</i> (mag)	<i>K</i> (mag)	Name ^a	Type
1	56.92333	+32.86216	8.75 ± 0.02	6.63 ± 0.02	3.58 ± 0.02	17.34 ± 0.26	14.05 ± 0.04	11.21 ± 0.02	B5 IRS 1	Class I
2	56.94643	+33.06756	8.79 ± 0.02	7.82 ± 0.02	5.53 ± 0.02	12.17 ± 0.03	11.02 ± 0.03	10.22 ± 0.03	B5 IRS 4	Class II
3	56.90464	+33.09548	13.33 ± 0.03	13.03 ± 0.03	10.84 ± 0.11	16.35 ± 0.11	14.55 ± 0.05	13.66 ± 0.04	This work	Class II
4	56.73645	+32.88013	14.00 ± 0.03	12.89 ± 0.03	9.81 ± 0.05	17.12...	16.13 ± 0.20	15.12 ± 0.12	SSTc2d J034656.7+325248	Class I
5	56.73914	+32.82148	11.82 ± 0.02	11.33 ± 0.02	9.92 ± 0.07	13.57 ± 0.02	12.73 ± 0.02	12.31 ± 0.02	2MASS J03465739+3249173	Class II
6	56.74386	+32.78301	11.81 ± 0.02	11.36 ± 0.02	9.95 ± 0.06	13.58 ± 0.02	12.61 ± 0.02	12.16 ± 0.02	2MASS J03465851+3246588	Class II
7	56.74576	+32.75514	13.85 ± 0.03	12.08 ± 0.03	9.01 ± 0.03	Infrared source	Class I
8	56.77269	+32.71899	9.60 ± 0.02	8.22 ± 0.02	5.72 ± 0.02	16.41 ± 0.15	14.26 ± 0.06	12.05 ± 0.02	B5 IRS 3	Class I
9	57.12281	+32.65460	13.40 ± 0.03	13.14 ± 0.03	11.75 ± 0.28	14.52 ± 0.03	13.86 ± 0.03	13.59 ± 0.04	This work	Class II
10	57.33036	+32.87553	13.68 ± 0.03	13.38 ± 0.04	11.76 ± 0.24	This work	Class II
11	57.36914	+32.96846	13.50 ± 0.03	13.22 ± 0.03	11.86 ± 0.30	14.89 ± 0.03	14.16 ± 0.04	13.83 ± 0.04	This work	Class II
12	57.45101	+33.00102	13.60 ± 0.03	13.34 ± 0.04	11.42 ± 0.20	14.85 ± 0.03	14.08 ± 0.03	13.80 ± 0.04	This work	Class II
13	56.86345	+32.50027	12.25 ± 0.03	11.62 ± 0.02	10.61 ± 0.10	14.39 ± 0.03	13.45 ± 0.03	12.79 ± 0.02	2MASS J03472722+3230010	Class II
14	56.87431	+32.49139	13.63 ± 0.03	13.38 ± 0.04	11.31 ± 0.23	14.91 ± 0.03	14.15 ± 0.04	13.84 ± 0.04	This work	Class II
15	57.50904	+33.08623	13.96 ± 0.03	13.43 ± 0.04	10.47 ± 0.08	15.44 ± 0.05	14.71 ± 0.05	14.34 ± 0.06	This work	Class II
16	57.12943	+32.43432	13.66 ± 0.03	12.53 ± 0.03	9.66 ± 0.06	This work	Class I

Note.

^a Please see Section 4 for further details about the individual targets.

Table 4
Gaia EDR3 Data of Young Stellar Objects

α_{J2000} (deg)	δ_{J2000} (deg)	ϖ (mas)	μ_{α} (mas yr ⁻¹)	μ_{δ} (mas yr ⁻¹)	G (mag)	G_{BP} (mag)	G_{RP} (mag)	Name
57.0973	+33.0194	2.41 ± 0.06	3.71 ± 0.09	-5.42 ± 0.05	15.73 ± 0.004	17.44 ± 0.02	14.33 ± 0.01	Candidate YSO (Zari et al. 2018)
57.2800	+33.0390	2.30 ± 0.08	3.84 ± 0.10	-4.86 ± 0.07	16.90 ± 0.003	19.29 ± 0.03	15.50 ± 0.01	Candidate YSO (Zari et al. 2018)
57.3692	+32.9684	2.47 ± 0.26	3.35 ± 0.33	-4.73 ± 0.21	18.99 ± 0.003	21.33 ± 0.11	17.52 ± 0.01	Source No. 11
57.0977	+33.0193	2.61 ± 0.14	2.91 ± 0.28	-5.03 ± 0.25	Candidate YSO (Zari et al. 2018)
57.4510	+33.000	2.62 ± 0.21	3.00 ± 0.27	-5.36 ± 0.17	18.61 ± 0.003	20.86 ± 0.13	17.17 ± 0.01	Source No. 12
WISE and 2MASS Targets, Gaia Counterparts								
56.9464	+33.0675	4.77 ± 0.29	1.21 ± 0.40	-4.17 ± 0.22	15.77 ± 0.01	16.93 ± 0.02	14.32 ± 0.02	B5 IRS 4
56.7391	+32.8215	18.34 ± 0.01	19.67 ± 0.04	16.08 ± 0.01	Source No. 5 ^a
56.7439	+32.7830	17.88 ± 0.01	20.39 ± 0.07	16.27 ± 0.01	Source No. 6 ^a
57.1229	+32.6545	7.97 ± 0.14	73.70 ± 0.16	-5.73 ± 0.10	17.77 ± 0.003	19.65 ± 0.04	16.46 ± 0.01	Source No. 9 ^a
57.3304	+32.8755	15.28 ± 0.25	-64.27 ± 0.32	-337.94 ± 0.19	18.62 ± 0.003	21.44 ± 0.12	17.12 ± 0.01	Source No. 10 ^a
56.8635	+32.5002	2.24 ± 0.34	3.52 ± 0.40	-5.76 ± 0.28	19.40 ± 0.02	21.03 ± 0.11	17.85 ± 0.06	Source No. 13 ^a
56.8743	+32.4914	3.56 ± 0.17	23.87 ± 0.19	-8.07 ± 0.14	18.45 ± 0.003	20.43 ± 0.08	17.07 ± 0.01	Source No. 14 ^b
57.5090	+33.0862	2.57 ± 0.32	3.05 ± 0.37	-4.56 ± 0.28	19.42 ± 0.004	21.43 ± 0.14	17.96 ± 0.01	Source No. 15 ^b
57.1294	+32.4343	0.031 ± 0.28	-0.36 ± 0.31	-0.32 ± 0.24	19.10 ± 0.01	19.46 ± 0.03	18.32 ± 0.02	Source No. 16 ^a

Notes.

^a These sources have Gaia counterparts either with no proper-motion data or with a large error.

^b Source No. 14 and Source No. 15 are slightly outside our Gaia field, but both are within our proper-motion criterion.

literature and spectroscopically identified substellar objects in IC 348.

3.1.1. Spectral Fitting

We compared our spectra with library templates for spectral typing. Those for field brown dwarfs are taken from the SpeX library (Cushing et al. 2005; Rayner et al. 2009), whereas spectra for young brown dwarfs are adopted from Luhman et al. (2017). Each standard star belongs to one of the three age groups: VL-G (very low gravity ≈ 1 Myr), INT-G (intermediate gravity, with two subgroups: I for 10 Myr and Y for 5 Myr), or FLD-G (gravity for much older field stars). The data are dereddened by A_V ranging from 0 to 40 mag, using the reddening law from Fitzpatrick (1999). For further details on spectral classification, please see Dubber et al. (2021).

Spectra of young objects later than M5 show a characteristic inverted “V” (triangular) shape in the H band (Cushing et al. 2005). This feature, where H band is dominated by the strong water absorption bands peaking around $1.70 \mu\text{m}$, was first reported by Lucas et al. (2001) to be seen in young cool objects. The triangular peak in the H band is attributed to the effect of low-pressure and low-gravity atmospheres (Lucas & Roche 2000; Allers et al. 2007; Allers & Liu 2013). We found three new substellar objects in IC 348 with spectral type $\geq M5$, placing them at the boundary of the substellar regime (see Figures 7(a), (b), and (c), and Table 1).

In B5, the source 03481542+3309185 has a spectral type of $M4 \pm 0.5$ and can be fitted by either a field or a young template. According to the spectral classification of Zhang et al. (2018), this object has a spectral type of $M5.2 \pm 0.9$ and is a low surface gravity object (VL-G). This source therefore could be either a field or a young substellar object. The source 03492858+3258064 is the first confirmed brown dwarf toward B5 (see Figure 7(d) and Table 1). Three targets were too faint to be observed with IRTF/SpeX, so we refer to them as brown dwarf candidates (see Table 2). The newly identified substellar

objects in IC 348 and B5 are summarized in Table 1. Column (1) gives the ID in the water-band survey, followed by the coordinates in Columns (2) and (3). In Columns (4) and (5) we list the J - and H -band magnitudes measured by the CFHT/WIRCam. Column (6) gives the WISE W1 and W2 bands. Column (7) gives the difference between z band in Pan-STARRS and J_{CFHT} . The W -band data, along with J - and H -band magnitudes, lead to the derived Q parameter in Column (8) (see Equation (1)), used to identify brown dwarf candidates. Columns (9) and (10) give the spectral type and A_V obtained from spectral fitting. In Column (11) the age estimation is based on the spectral fitting mentioned above. The bolometric correction needed to calculate L_{bol} in Column (12) and T_{eff} in Column (13) is taken from Filippazzo et al. (2015; for spectral type M7 or later) or Herczeg & Hillenbrand (2014; earlier than M7), depending on the spectral type of the object.

3.1.2. Physical Properties

We infer the range of age and mass of each confirmed substellar object with the evolutionary tracks from Baraffe et al. (2015). The bolometric magnitudes and the effective temperatures (T_{eff}) for our targets were determined using the technique described in Section 6.4 of Dubber et al. (2021). In a nutshell, we used the CFHT photometry and created a grid of SpT- A_V probability maps to calculate the bolometric magnitude and luminosity. Each point in the grid has a χ^2 value associated, which we convert into a normalized probability. Monte Carlo analysis was performed, using 500,000 model objects and distributed proportionally across the SpT- A_V grid using the probability for each bin. For each simulated object of each SpT- A_V probability bin, we calculated the bolometric magnitude (using Equation (4) in Dubber et al. 2021) by sampling Gaussian distributions of distance modulus d_{mod} and apparent magnitude m_J . The Gaussian distribution of m_J is created using the CFHT apparent magnitude and error.

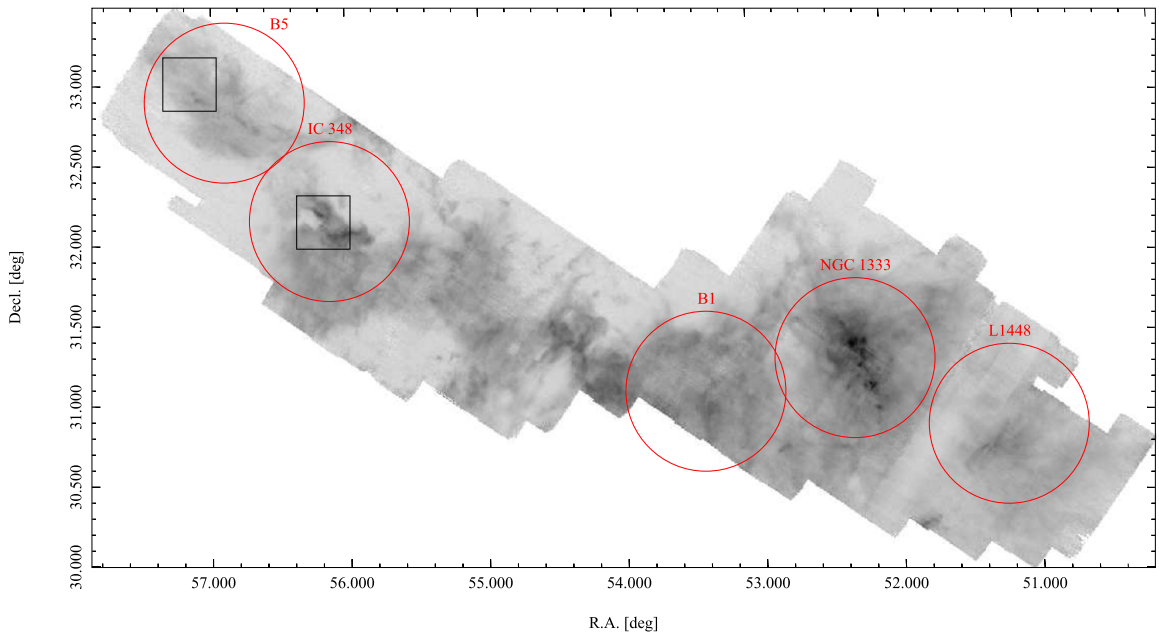


Figure 1. ^{12}CO ($J = 1 - 0$) FCRAO data of the Perseus molecular cloud (Ridge et al. 2006a). The black squares show the fields toward IC 348 and B5 covered by the W-band imaging survey. The red circles mark the fields of $\sim 30'$ radius analyzed by using Gaia EDR3 data, including three other regions, Barnard 1, NGC 1333, and L1448 (see Section 4 for further details).

Table 5
Proper Motion and Parallax of Regions of the Perseus Molecular Cloud

Region	α_{J2000} (deg)	δ_{J2000} (deg)	μ_{α} (mas yr $^{-1}$)	μ_{δ} (mas yr $^{-1}$)	ϖ (mas)	$1/\varpi$ pc
Barnard 5	56.90	32.90	4.00 ± 0.94	-5.32 ± 0.67	2.35 ± 0.76	426 ± 32
IC 348 (Group A)	56.13	32.16	4.43 ± 0.20	-6.27 ± 0.14	3.14 ± 0.18	318 ± 37
IC 348 (Group B)	56.13	32.16	6.51 ± 0.28	-9.99 ± 0.21	3.19 ± 0.23	313 ± 47
Barnard 1	53.32	31.13	7.03 ± 0.16	-8.31 ± 0.12	3.23 ± 0.14	311 ± 40
NGC 1333	52.30	31.31	7.10 ± 0.17	-9.92 ± 0.12	3.41 ± 0.14	292 ± 47
L 1448	51.29	30.68	8.39 ± 0.10	-8.22 ± 0.07	3.37 ± 0.08	297 ± 62

We adopt the bolometric correction BC_J for a spectral type earlier than M7 (Herczeg & Hillenbrand 2015), or for an M7 or later (Filippazzo et al. 2015). We obtain bolometric luminosity (L_{bol}/L_{\odot}) using Equation (5) in Dubber et al. (2021) by converting the bolometric magnitude to bolometric luminosity. We convert this grid of (L_{bol}/L_{\odot}) into histogram distributions and find the peak with errors derived from the 68% Bayesian credible interval. The effective temperature (T_{eff}) plotted here is estimated using the derived spectral type and relations given in Table 5 of Herczeg & Hillenbrand (2014). Figure 8 exhibits the results for the brown dwarfs in IC 348 and in B5 in the H-R diagram.

As a separate analysis, we constructed the color-magnitude diagram for each region and compared the AMES-Cond and AMES-DUSTY models (Allard et al. 2001) to estimate the age of the substellar objects. This is displayed in Figure 9. In IC 348, two out of three brown dwarfs are consistent with an age of ~ 5 Myr, regardless of the Cond or the Dusty model. Here the isochrones are adjusted by a distance modulus of 7.46 mag and an extinction/reddening of $E(B - V) = 0.71$ mag (Trullols & Jordi 1997). In B5, the distance modulus of 7.72 mag is adopted, but the extinction to the cloud is unclear, so three different values of $E(B - V)$ are exercised, at 0, 0.5, and 1.0 mag. The single brown dwarf in B5 seems to fit well with an age of 5 Myr and a mild extinction of $E(B - V) = 0.5$ mag.

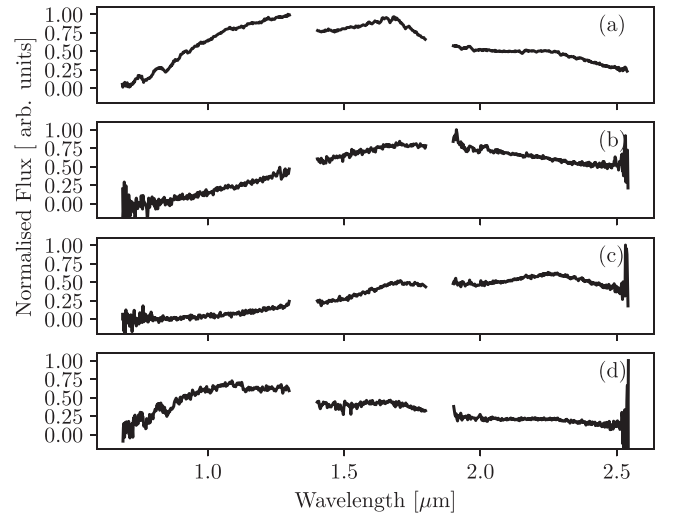


Figure 2. The observed flux-calibrated and normalized IRTF/SpEx spectra of the targets in IC 348: (a) 03434538+3201041, (b) 03435016+3204073, (c) 03441864+3218204, and (d) 3441864+3218204.

The age of IC 348 has been estimated in the literature to be 1–6 Myr (Luhman et al. 2003; Bell et al. 2013; Cottar et al. 2014), and the three newly identified substellar objects indeed

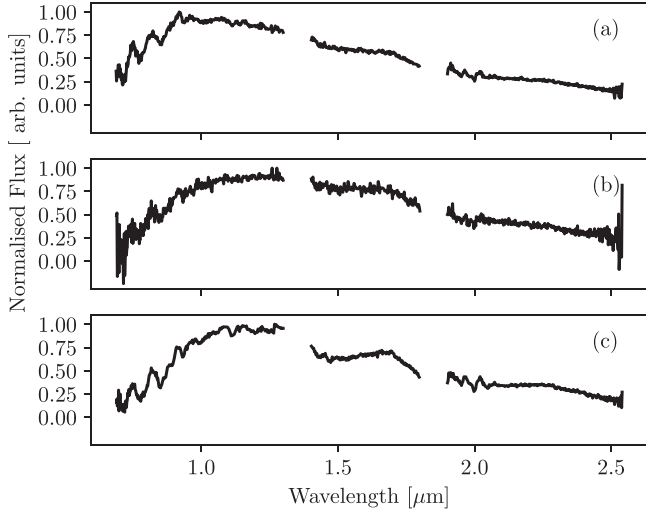


Figure 3. The observed flux-calibrated and normalized IRTF/SpeX spectra of the targets in Barnard 5: (a) 0348154+330918, (b) 0348362+325905, and (c) 0349286+325806.

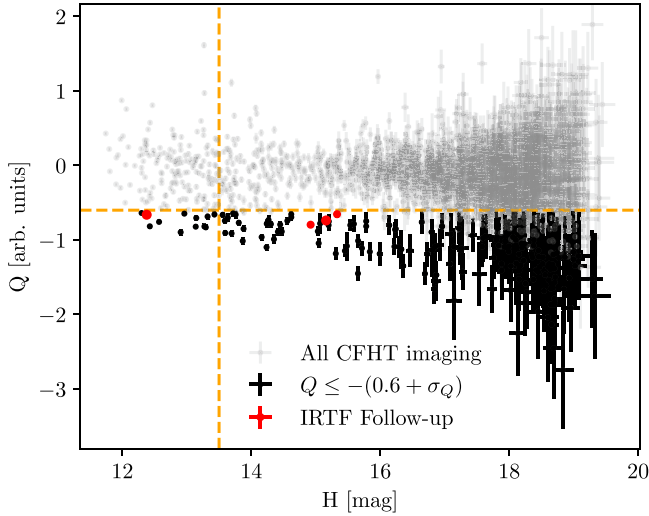


Figure 4. The Q index vs. H magnitude in IC 348. Of the total 1943 sources (in gray), those likely to exhibit flux suppression due to water absorption, i.e., with $Q + \sigma_Q \leq -0.6$, are marked in black (163 targets) with error bars. Those selected for spectroscopic follow up are represented in red. The orange dashed line of $H = 13.5$ mag indicates the nominal photometric saturation limit, whereas the one with $Q = -0.6$ denotes the substellar boundary for young objects. Note that the targets selected for spectroscopic follow up satisfy the water absorption and cool temperature criteria, i.e., $(W1-W2) > 0.10$ and $(z_{PS1} - J_{CFHT}) \leq 2$.

follow approximately the age range; it is assuring also that all the targets have masses close to the stellar/substellar boundary, i.e., $\lesssim 0.1 M_{\odot}$.

The source 03435016+3204073 in IC 348 lies above the 0.5 Myr isochrone in Figure 8; therefore, we cannot determine its mass or age reliably. A possible reason might be that it is a reddened very low mass star or a brown dwarf binary. The same source appears also highly reddened in Figure 9. It is interesting that its $J-H$ versus J location resembles that of a blackbody (Burrows et al. 1997). The nature of this object deserves further delineation.

In B5, the newly identified brown dwarf has an isochrone age of ~ 5 Myr and a mass of $0.05 M_{\odot}$. This is the first discovery of a brown dwarf to date toward B5 to our

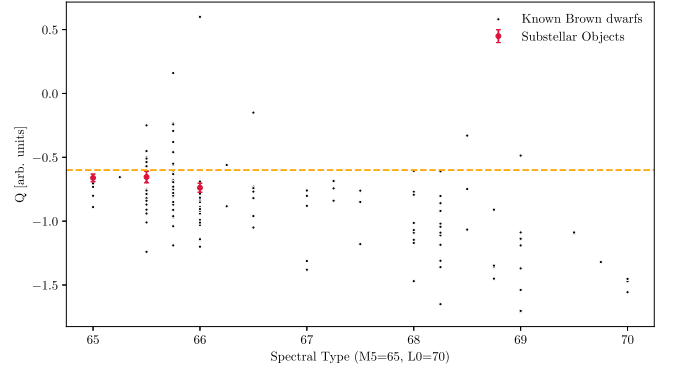


Figure 5. Spectral type vs. Q index of all known brown dwarfs in IC 348. The known brown dwarf list is taken from Muench et al. (2007), Luhman et al. (2016), and Alves de Oliveira et al. (2013). New discoveries from this work (confirmed spectroscopically), i.e., substellar objects, are shown in red with respective error bars. The orange dashed line denotes $Q = -0.6$, below which the Q value indicates a spectral type later than M6, corresponding to a substellar boundary for young objects.

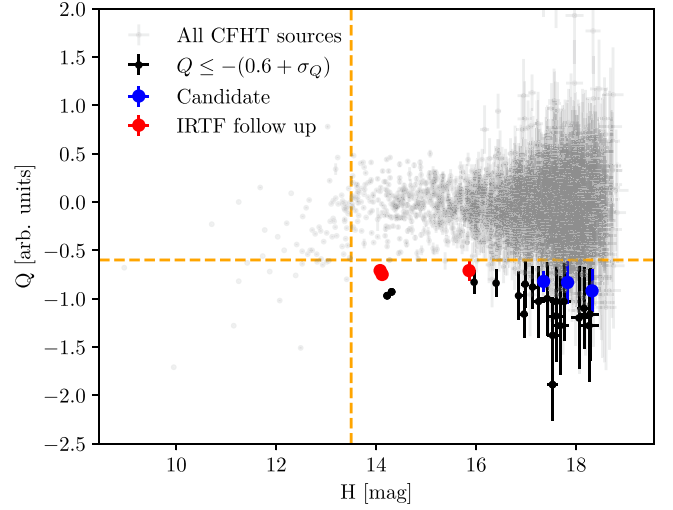


Figure 6. The Q index vs. H as in Figure 4 but for Barnard 5 (here with 2089 sources in gray). The black symbols mark those satisfying criteria of $Q \leq -(0.6 + \sigma_Q)$ and $H > 13.5$ mag (23 targets). The red symbols mark candidates that have been followed up spectroscopically with IRTF/SpeX, and the blue symbols show candidates too faint to be observed with IRTF/SpeX. Note that both the red and blue symbol targets satisfy the water absorption and cool temperature criteria, i.e., $(W1-W2) > 0.10$ and $(z_{PS1} - J_{CFHT}) \leq 2$.

knowledge. The age group assigned to this confirmed brown dwarf is INT-G (≈ 10 Myr), which may imply that this object is likely to be a young interloper, possibly slightly closer to us than B5. Studies of such widely distributed young low-mass objects from the previous generation of newly formed stars is seen in the Orion cloud complex, and it is possible to see such a distribution in the Perseus complex.

3.2. Selection of Young Stellar Members In B5 Using WISE and 2MASS

We adopted the scheme given by Koenig & Leisawitz (2014), i.e., with color cuts from W1 to W3 for different YSO classes, and removing possible contaminants such as active galactic nuclei and star-forming galaxies. Using the $(W1-W2)$ versus $(W2-W3)$ diagram, we identified five Class I and 11 Class II candidates, as shown in Figure 10(a).

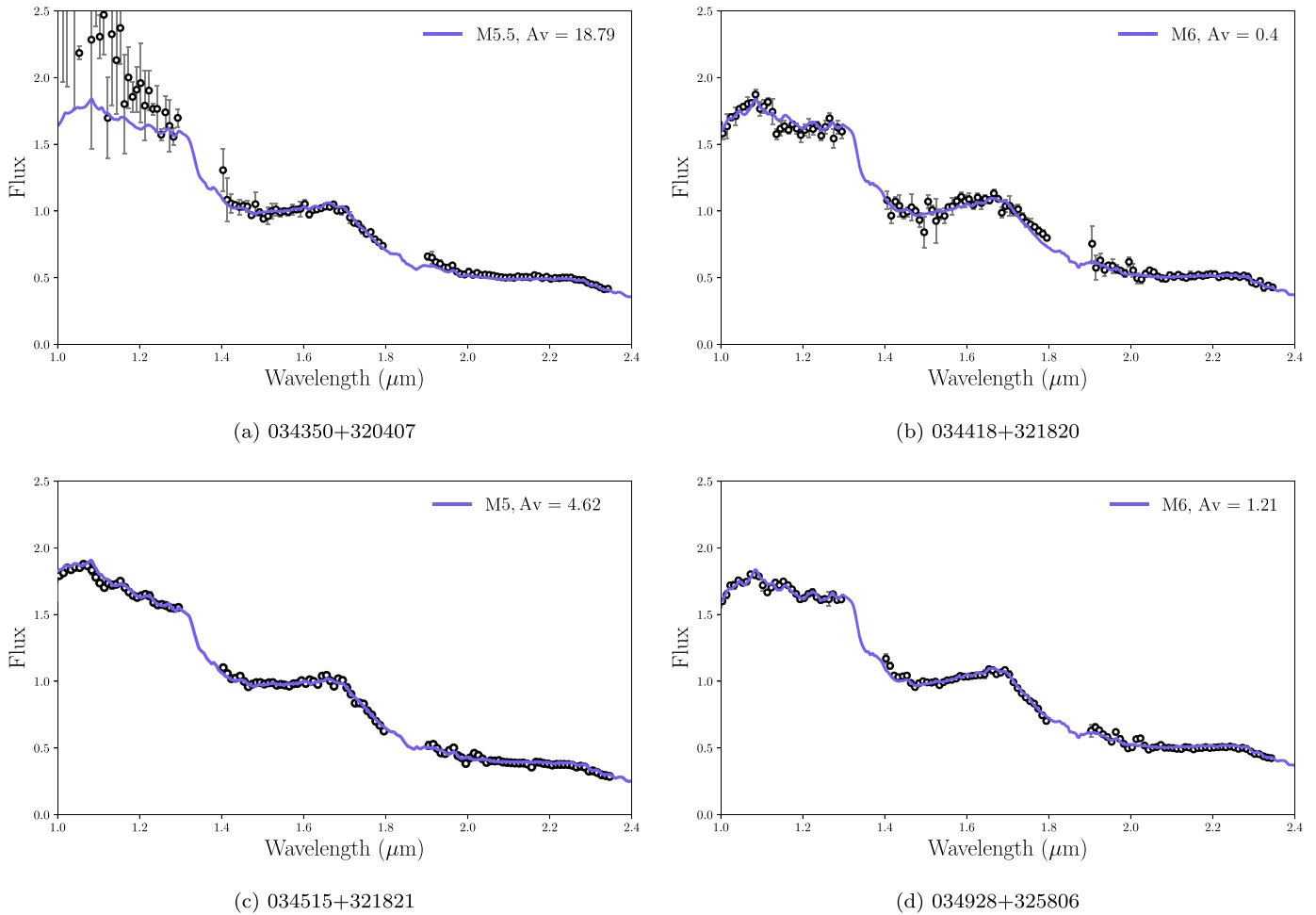


Figure 7. The dereddened spectra (in black) of the three candidates in IC 348 are shown in panels (a), (b), and (c), and one in B5 is shown in panel (d), with the best-fit template (in purple) shown in each case.

There are 1985 2MASS sources with quality flag “AAA.” Of the YSO candidates found by the WISE colors, Nos. 7 and 16 (both Class I) and No. 10 (Class II) in Table 3 have no 2MASS counterparts, whereas three out of five Class I and 10 out of 11 Class II sources have reliable 2MASS measurements, allowing us to conduct a consistency check of their youth nature, depicted in Figure 10(b). Two of the Class II candidates, Nos. 2 and 13 in Table 3, have consistent 2MASS colors with being T Tauri stars, whereas the rest lie along the giant loci. No. 11 as a Class II candidate has a counterpart in our CFHT images and was selected as a Q candidate for a follow-up spectroscopy. The target 03492858+3258064 turns out to be the first confirmed brown dwarf in B5.

3.3. Kinematics of IC 348 and B5

The proper-motion vector plot of IC 348 displayed in Figure 11(a) shows two distinct groups, one (Group A) centering around $\mu_\alpha = 4.43 \text{ mas yr}^{-1}$ and $\mu_\delta = -6.27 \text{ mas yr}^{-1}$ and the other (Group B) around $\mu_\alpha = 6.51 \text{ mas yr}^{-1}$ and $\mu_\delta = -9.99 \text{ mas yr}^{-1}$. The two kinematic groups are also distinguished in parallax and in sky position (Figures 11(b) and 11(c)). Group A is bimodal in the parallax distribution, as illustrated in Figure 11(b), peaking near 0.5 mas, coincident with the field distribution and another more populous one that peaks at 3.1 mas. Group B contains less stars but also exhibits

two maxima at about the same parallax values as above. The positional distribution clarifies the origin of each kinematic group, namely, Group A is by and large centrally concentrated, i.e., the cluster of IC 348 itself, whereas stars in Group B are dispersed throughout the field. The reciprocal of the mean parallax of Group A (3.1 mas), 323 pc, is consistent with the distance to IC 348 (Ortiz-León et al. 2018), confirming that Group A is the cluster, whereas a fraction of Group B, the ones at similar distances, is the general young stellar population permeating the Perseus complex.

For B5, adopting the coordinates given by Pezzuto et al. (2021), we see no well-defined grouping in proper motion in Figure 12(a), unlike that in IC 348. We cross-matched the list of young stellar population members known in the literature (i.e., SIMBAD) with Gaia EDR3 sources (Gaia Collaboration et al. 2021), within a coincidence radius of $5''$, resulting in 12 objects classified as “YSO,” or a candidate “YSO.” In the parallax distribution of the young stellar objects (YSOs), there is a peak within a narrow range between 2.0 and 2.6 mas (see Figure 12(b)). We have listed only those YSOs that are within the given parallax range in Table 4. The mean parallax and proper motion are 2.35 mas and $\mu_\alpha = 4.00 \text{ mas yr}^{-1}$, $\mu_\delta = -5.32 \text{ mas yr}^{-1}$ (see Table 5), respectively. The reciprocal of the mean parallax corresponds to a distance of 426 pc, therefore placing it farther away than the value of 350 pc suggested by Herbig & Jones (1983) or Dickman (1978).

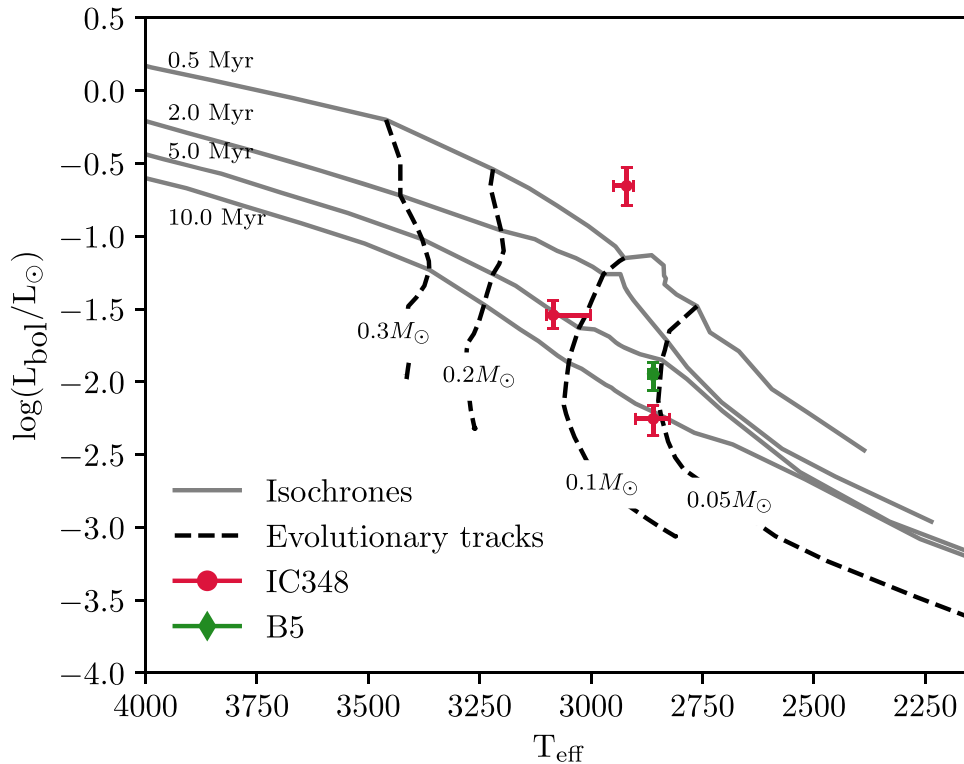


Figure 8. H-R diagram for IC 348 (red) and B5 (green) brown dwarfs overlapped with the isochrones (solid lines; 0.5–10 Myr) and evolutionary tracks (dashed lines; 0.05–0.3 M_{\odot}) from Baraffe et al. (2015), from where the mass and age are inferred.

4. Individual Young Stellar Objects in B5

We look for additional evidence of youth by using the WISE and 2MASS colors. A total of 16 YSOs are found, of which one Class I object and seven Class II objects are newly found. They are listed in Table 3, in which a sequence number, the coordinates, and WISE and 2MASS magnitudes are given, followed by the name known in the literature, if any, and the classification of the object.

Beichman et al. (1984) reported four IRAS sources in the vicinity of B5, among which IRS 1 (IRAS 03445+3242) is the youngest and the first embedded YSO. Located near the center of the cloud, the source (No. 1 in Table 3) is very cold, with temperature and luminosity being 30–100 K and $10 L_{\odot}$, respectively (Beichman et al. 1984), and associated with CO outflows (Zapata et al. 2014), bow shocks, Herbig-Haro objects (HH 366E and HH 366W; Bally et al. 1996; Yu et al. 1999), and shock-excited H_2 emissions. IRS 1 has a circumstellar disk whose orientation is perpendicular to the CO outflow (Fuller et al. 1991; Langer et al. 1996) and also exhibits a highly collimated optical jet (Bally et al. 1996). $NH_3(1,1)$ and $(2,2)$ observations with the Jansky Very Large Array (Pineda et al. 2015) additionally revealed the presence of filaments within the quiescent dense core. These filaments enclose three high-density bound condensations that, combined with IRS 1, might form a bound quadruple multiple-star system (Pineda et al. 2015). The WISE and 2MASS colors of IRS 1 suggest all consistency with a Class I object.

Source No. 2 in (Table 3) is IRS 4 (IRAS 03446+3254), to the northeast of B5, and is the most evolved known YSO in B5 (Goldsmith et al. 1986; Langer et al. 1989; Yu et al. 1999). Molecular line maps show a large cavity having a diameter of $6'$ (Goldsmith et al. 1986; Langer et al. 1989; Arce et al. 2011), likely tracing a much older outflow. This target has WISE Class II colors

and 2MASS colors consistent with being a mildly reddened classical T Tauri star.

Source No. 3 was not previously identified in the literature. We have classified it as a possible Class II, or a reddened dwarf.

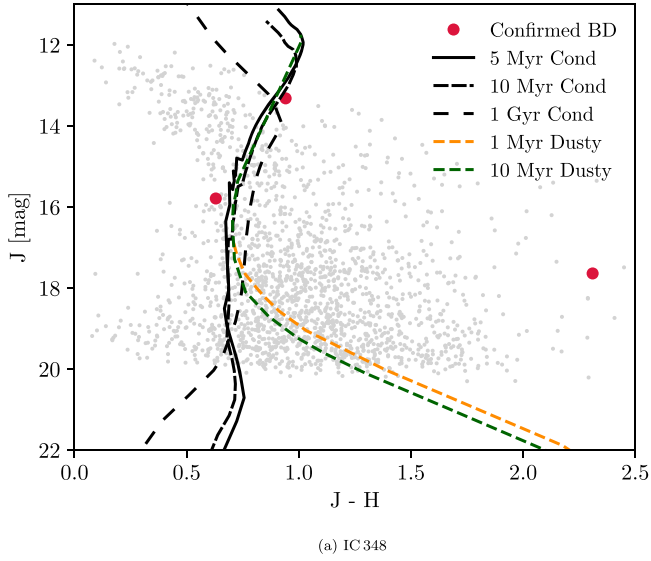
Source No. 4, SSTc2d J034656.7+325248, was identified by Dunham et al. (2008) as a low-luminosity Class I protostar with $0.015 L_{\odot}$ based on 3.6–70 μm Spitzer data. This target is a WISE Class I and is very close to the 2MASS classical T Tauri loci.

Both Source No. 5 and Source No. 6 were identified as Class II YSOs by Dunham et al. (2015), Young et al. (2015), and Evans & Dunham (2009) based on 3.6–24 μm Spitzer data, with the extinction-corrected luminosity of $0.039 L_{\odot}$ (Source No. 5) and $0.047 L_{\odot}$ (Source No. 6). In Figure 10(a) both sources appear close to each other, and in 2MASS both the targets appear together at the edge of the classical T Tauri loci.

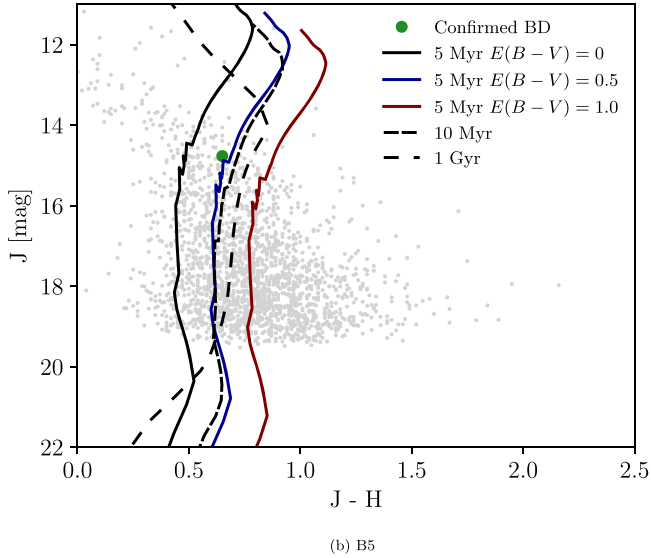
Source No. 7 is a known infrared source. The source does not have a 2MASS counterpart, with the WISE colors suggesting a reddened Class I YSO, though Hsieh & Lai (2013), based on Spitzer c2d data, have classified it as a probable galaxy contaminant. Source No. 8 is IRS 3 (IRAS 03439+3233) located toward the southwest of IRS 1 and drives small-scale Herbig-Haro objects, HH 367A and HH 367B, with HH 844 extending to the south (Walawender et al. 2005). This target is identified as a Class I object judging by both WISE and 2MASS colors.

Source No. 9 is classified marginally as a WISE Class II source, but in 2MASS the target is reddened and lies in the dwarf loci. Source No. 10 is also a marginal WISE Class II source. It does not have a 2MASS counterpart, and if reddening is considered, it could still be a Class II.

Source No. 11 is identified as a Class II object and has a counterpart in our CFHT images. This target was followed up



(a) IC 348



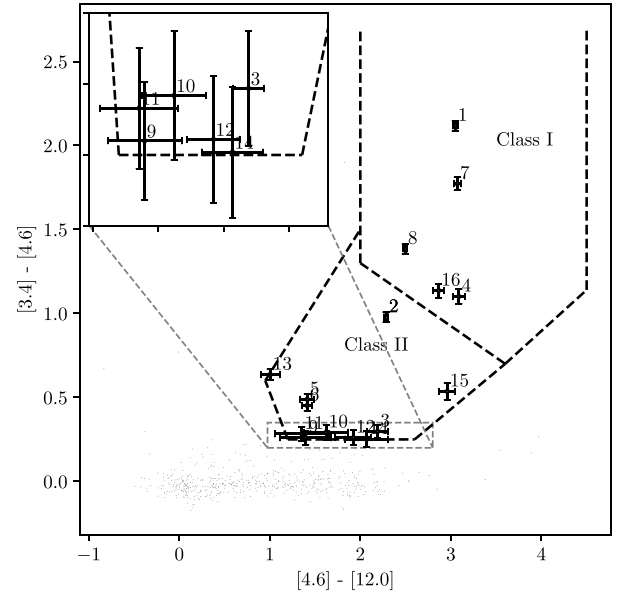
(b) B5

Figure 9. J vs. $J - H$ color-magnitude diagram for (a) IC 348 and (b) B5. The gray points represent all the CFHT WIRCam sources in the corresponding region, whereas the confirmed brown dwarfs for IC 348 (in red) and for B5 (in green) are marked. Isochrones from the AMES-Cond and AMES-DUSTY models (Allard et al. 2001) are overlapped, each adjusted by a distance modulus of 7.46 mag and $E(B - V) = 0.71$ (Trullols & Jordi 1997) for IC 348 and a distance modulus of 7.72 mag and $E(B - V) = 0.5, 1.0,$ or 1.5 for B5, assuming $R_V = A_V/E(B - V) = 3.1$ and the reddening law of $A_J = 0.277A_V,$ $A_H = 0.171A_V$ (Cardelli et al. 1989).

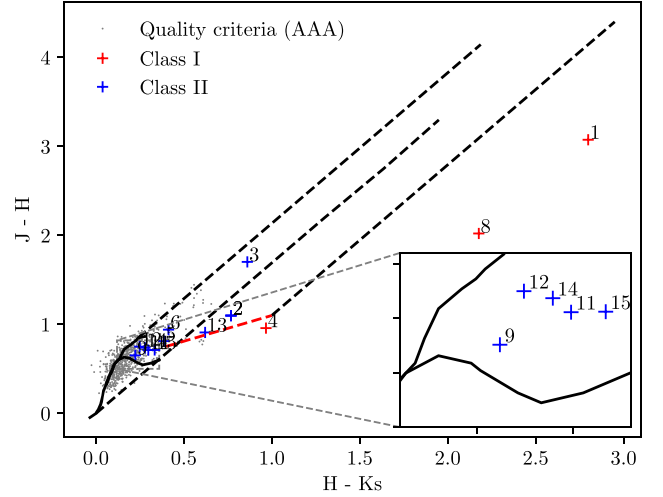
spectroscopically as a Q candidate brown dwarf in B5. In the 2MASS color-color plot this target lies near the dwarf loci. Source No. 12 is classified as a Class II object based on WISE colors, but in 2MASS the target lies in the main-sequence loci.

Source No. 13 is known as 2MASS J03472722+3230010. It is identified by Yao et al. (2018) as a disk-bearing source in IC 348. Considering its sky position, we associate it with B5 instead and classify it as a Class II object.

Source No. 14 is classified as a WISE Class II object. Source No. 15 appears to be more reddened than source No. 14. In 2MASS both the targets appear in the reddened dwarf loci. Source No. 16 is a WISE Class I object but does not have a 2MASS counterpart.



(a) WISE



(b) 2MASS

Figure 10. WISE and 2MASS color-color diagram toward B5. (a) WISE (W1-W2) vs. (W2-W3) color-color diagram to identify Class I and Class II objects by adopting the classification criteria given by Koenig & Leisawitz (2014). The black dots with their respective error bars have photometric quality flags “AAA” and “AAB.” The inset shows a zoom-in of all the targets that lie close to the boundary of Class II objects. (b) 2MASS ($H - K_s$) vs. ($J - H$) color-color diagram. The intrinsic loci of dwarfs and giants are each marked with a black curve (Bessell & Brett 1988), whereas those of classical T Tauri stars are represented by the dashed red line (Meyer et al. 1997). All the data points are transformed to the CIT system (Carpenter 2001). The dashed lines represent the reddening direction from the tips of the giants, dwarfs, and T Tauri loci, respectively. The Class I and Class II sources identified in panel (a) are labeled and plotted here with the same symbols. The inset shows a zoom-in of all the targets that lie close to the dwarf and main-sequence loci.

Note that of the four IRAS sources originally reported by Beichman et al. (1984), IRS 2 (IRAS 03449+3240) is colder (color temperature ~ 25 K) but much less luminous ($1.3 L_{\odot}$) than IRS 1. It was supposed to be either an internally powered prestellar core or an externally heated clump (Beichman et al. 1984). This source is not included in our YSO list because it is

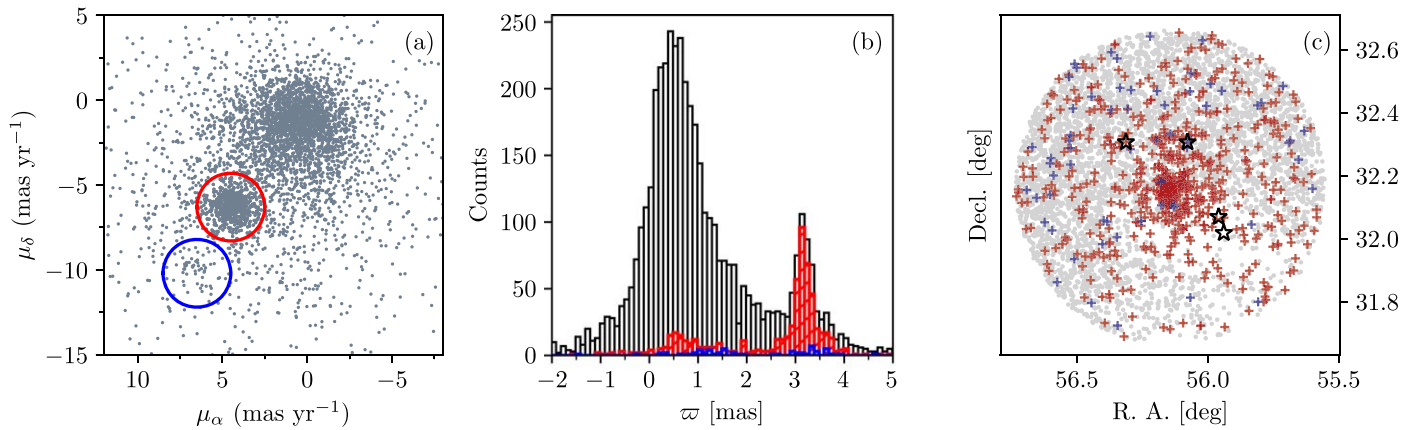


Figure 11. Gaia EDR3 30' field toward IC 348. (a) Proper-motion scatter plot (gray points), with two distinct groups marked with a red circle (Group A) and a blue circle (Group B), each with a radius of 2 mas yr⁻¹. (b) Parallax distribution of the stars in panel (a), with Group A shown in red and Group B in blue. Stars belonging neither in Group A nor in Group B, i.e., field stars, are represented in the gray histogram. (c) Sky positions of the stars in panel (a) using the same color scheme as in panel (b), that is, red for proper-motion Group A, blue for proper-motion Group B, and gray for stars in neither group. Additionally, the black symbols represent the three confirmed substellar objects and one contaminant.

highly reddened, $(W2-W3) = 4.8$, and therefore not categorized as any YSO class.

5. Bulk Motion of Perseus Subclusters

In addition to the study of B5 and IC 348 detailed above, we consider the Gaia EDR3 data of three other star-forming regions, namely, continuing westward, Barnard 1, NGC 1333, and L1448 (Barnard 203), together spanning across the Perseus molecular cloud. As in the analysis of IC 348, the kinematic grouping of each region is utilized to find the average proper motion and parallax. For each of the regions we analyzed the Gaia EDR3 data in a $\sim 30'$ Gaia EDR3 field (see Figure 1). This angular size of the field was not meant to be optimal but was considered sufficiently large to cover the entire region to recognize a reliable group of stars in the proper-motion distribution. In B5, no such distinct kinematic grouping is obvious, so a sample of young stars were utilized; the membership sample is small and within a narrow range of parallax (see Figure 12). Each of the remaining four regions exhibits a separate proper-motion grouping for which the average proper motion and parallax are computed. In every case a secondary peak exists that mimics the shape of the field distribution. The results of the Gaia EDR3 data for Barnard 1, NGC 1333, and L1448 are presented in Figure 13.

The IC 348 cluster experiences relatively low extinction but is surrounded by heavy filaments, delineated by the paucity of Gaia EDR3 stars in the south, where ongoing star formation is taking place (see Figure 11(c)). The other rich cluster, NGC 1333, in contrast coincides with the dense parts of the cloud and has a shape elongated NE-SW. L1448, on the other hand, seems to be offset to the north from the obscured patches. Barnard 1 appears marginally within our default 30' field, with the proper motion and parallax “candidate members” scattering throughout the field, with no spatial concentration. Gaia star counts reveal the same NW-SW dark filament direction as detected by Walawender et al. (2005).

Ortiz-León et al. (2018) reported detailed VLBA and Gaia DR2 astrometry for IC 348 and NGC 1333 and, with mean radial velocities, derived the 3D motion of the two clusters. For IC 348, our estimates of the average parallax of $\varpi = 3.14 \pm 0.1$ mas and of the proper motion of 4.4 ± 0.8 , -6.3 ± 0.7 mas yr⁻¹ agree within uncertainties with their Gaia parallax of

$\varpi_{\text{Gaia}} = 3.09$ mas, VLBA parallax of $\varpi_{\text{VLBA}} = 3.12$ mas, and proper motion of 4.35 , -6.76 mas yr⁻¹. For NGC 1333, our values are also consistent with those reported by Ortiz-León et al. (2018) based on Gaia DR2 measurements.

The overall motion and orientation of the Perseus cloud complex probed by the five selected regions are summarized in Table 5 and depicted in Figure 14. In our analysis we compared the parallax measurement of each cloud, rather than the distance itself, even though at this close distance the bias introduced in the reciprocal function in estimate of the distance (Bailer-Jones et al. 2021) is expected to be minimal. Our results support the earlier notion that the western complex is closer than the eastern part (Schlafly et al. 2014; Ortiz-León et al. 2018), and with a systematic trend in both proper motion and parallax extending further to include B5, the easternmost edge of the complex. While the near side is at some 300–320 pc (Pezzuto et al. 2021), B5 stands alone to be ~ 100 pc farther away.

For B5, Langer et al. (1989) concluded with the optically thin ¹³CO tracer to derive some 1000 M_{\odot} of gas and dust, comparable to the virial mass, with a relatively small fraction ($\sim 200 M_{\odot}$) in the core and fragments. Our YSO census within the 30' field using 2MASS and WISE should be reasonably complete down to the magnitude limits. Our W -band image, though limited in spatial coverage, led to the encouraging discovery of one brown dwarf. A survey more comprehensive than we reported here for the entire B5 cloud is desirable to further add to the substellar sample. In any case, given the few known YSOs, of which many are Class I objects, B5 appears to be in infancy in star formation and low in formation efficiency. The cloud subtends $\sim 1^{\circ}$ in the sky (Bensch 2006), which, adopting a distance of 400 pc, corresponds to a 7 pc linear dimension. B5 is certainly connected with the complex, witnessed in the continuation of the distribution of CO (see Figure 1) or the Herschel far-infrared data (Figure 4 in Ortiz-León et al. 2018). If so, the fact that B5 stretches a depth (100 pc) more than the length scale projected on the sky plane suggests a bending morphology, alongside or on the backside of the Per OB2 bubble, of this part of the complex.

Massive stars upon birth interact and impact the neighboring environments. They may disrupt a nearby cloud to hamper any star formation activity. At a distance, however, these luminous

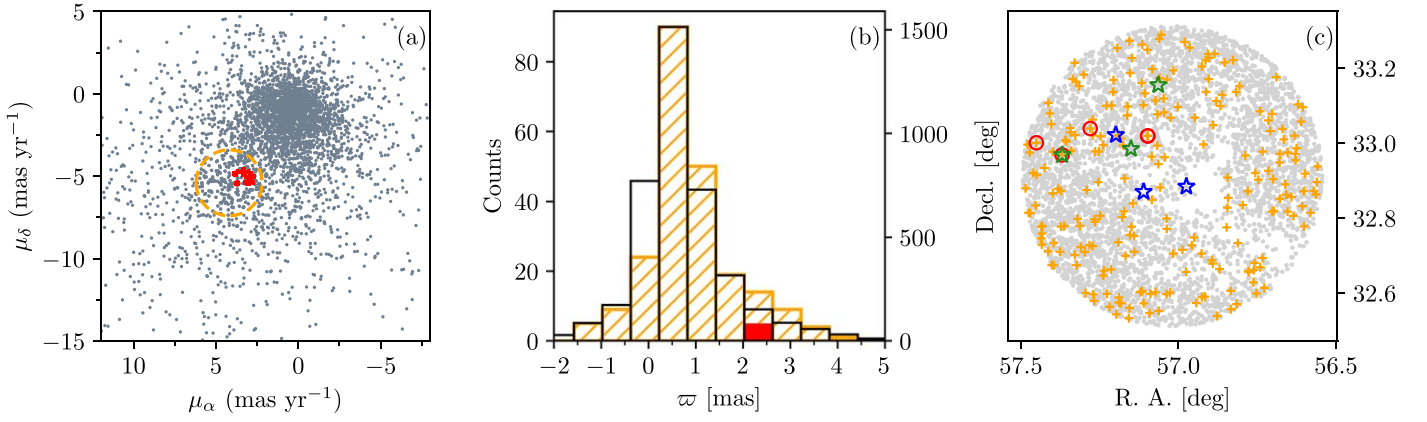


Figure 12. Same as Figure 11, but for Barnard 5. (a) In the proper-motion vector plot (gray points) the red symbols mark known YSOs, and the orange circle shows a radius of 2 mas yr⁻¹ to encompass the possible range of proper motion. (b) The parallax distribution of the YSOs (in red) and of the stars within the orange circle in panel (a) but excluding the YSOs (in orange). Both the red and orange histograms use the ordinate scale on the left. All other stars outside the orange circle in panel (a) are shown as the black histogram and use the ordinate scale on the right. (c) The sky position of the three kinds of stars as in panel (b), with the same color scheme. Additionally, the blue symbols represent brown dwarf candidates, and the green symbols represent confirmed brown dwarf and the contaminants.

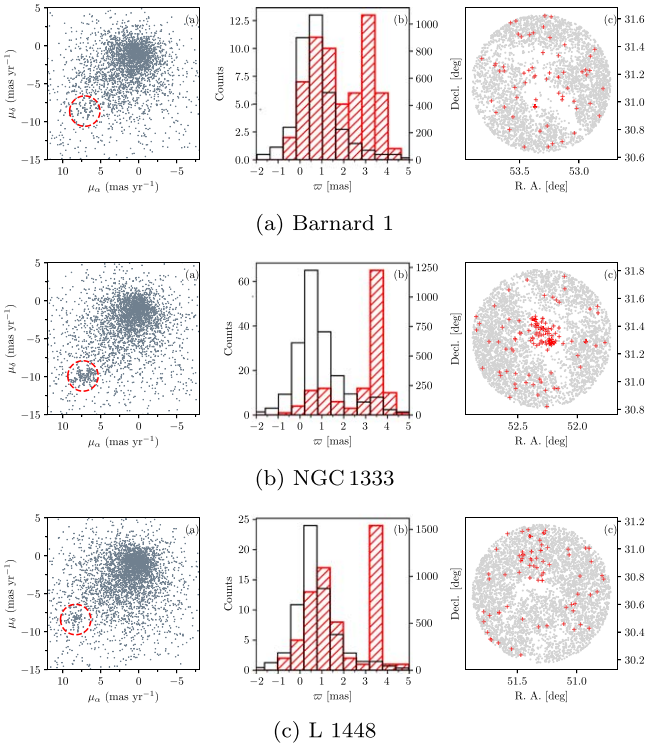


Figure 13. Same as Figure 11, but for the three star-forming regions of the Perseus molecular cloud.

stars via their winds and radiation could instead play a constructive role in compressing a cloud, thereby prompting the formation of the next generation of stars (Lee et al. 2005; Chen et al. 2007; Lee & Chen 2007). A supernova explosion has an even longer-range effect and produces a cavity that plows into an ever-denser expanding shell of gas and dust, within which gravitational instability then leads to the formation of giant molecular clouds that fragment hierarchically to form stellar groups (McCray & Kafatos 1987). Such a “collect-and-collapse” process can propagate on large (> 100 pc) scales, and indeed embedded star clusters are detected at the peripheral shells/rings of some H II regions (Zavagno et al. 2006). Differing timing of the explosive or

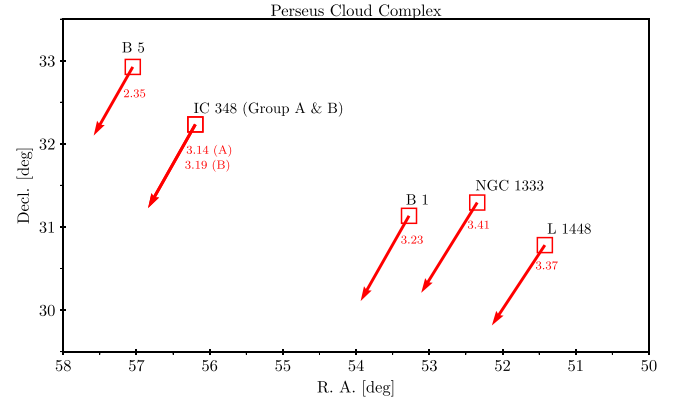


Figure 14. Proper motion and parallax distribution of the selected regions in the Perseus complex. Each red square marks the sky position of a region, with an arrow illustrating the relative proper motion (not to scale with the coordinate axes). The number next to the square denotes the average of the parallax values (given in mas).

photoionization shock fronts encountering the surrounding clouds, plus possibly multiple supernova events in an OB association, results in an age spread in the YSOs thus induced to form. It has been suggested that Perseus OB2 (Per OB2) has such an influence in triggering the star formation in the Perseus cloud complex.

Per OB2, located at a distance of ~ 300 pc, is one of the major OB associations in the solar vicinity (de Zeeuw et al. 1999). Supernova explosion in Per OB2 drives an expanding H II supershell with a diameter of $\sim 20^\circ$ into the surrounding interstellar medium (Sancisi et al. 1974; Heiles 1984; Hartmann & Burton 1997). The eastern end of the Perseus cloud being close to the centroid of the HI (de Zeeuw et al. 1999; Ridge et al. 2006b; Bally et al. 2008).

Comparatively, the cluster NGC 1333, together with the associated reflection nebula and dark cloud L1450 (Barnard 205), is the most rigorous star-forming region in the Perseus complex, manifest amply with embedded submillimeter cores, protostellar jets/outflows, and shock-excited HH objects. With an estimated age of ~ 1 Myr, the total stellar mass of $\sim 100 M_\odot$ signifies a star formation rate of $10^{-4} M_\odot \text{ yr}^{-1}$ (Walawender et al. 2008). Except for the cluster IC 348 representing the earlier epoch of star birth, the current episode

of star formation appears to pervade throughout the complex, including the regions we present in this work.

6. Conclusion

We present results from the *W*-band survey to search for brown dwarfs in IC 348 and B5, as well as broadband infrared colors to find young stars in B5. Our main results are as follows:

1. *W*-band imaging, devised to detect the water absorption feature commonly seen in substellar objects, continues to demonstrate its effectiveness, providing a high positive rate of 90% for follow-up confirmation spectroscopy, to filter out reddened background sources. This work applied this technique to two clouds at the eastern edge of the Perseus star-forming complex.
2. We found three previously unknown substellar objects in IC 348, enhancing the substellar sample in addition to the relatively well known stellar membership in the cluster.
3. Barnard 5 appears to be isolated with a low level of star-forming activity. Our *W*-band images covering part of the cloud led to the discovery of the first brown dwarf in this region. Using WISE and 2MASS data, we identified 16 YSOs, of which one new Class I and seven Class II objects were previously unknown. Barnard 5 should be at the initial stage of star birth, not necessarily as influenced by the neighboring Per OB2 as is the case for IC 348.
4. Using the Gaia EDR3 data of five selected star-forming regions in the complex, we derived the distances of L1448, NGC 1333, Barnard 1, and IC 348, progressively more distant from southwest to northeast, in the range of 300–320 pc. The Barnard 5 cloud, however, is found to be considerably farther at ~ 426 pc.

B.L. and W.-P.C. acknowledge financial support from the MOST grant 109-2112-M-008-015-MY3 to carry out this study. Based on observations obtained with WIRC*am*, a joint project of CFHT, Taiwan, Korea, Canada, and France, at the Canada–France–Hawaii Telescope (CFHT), which is operated by the National Research Council (NRC) of Canada, the Institut National des Sciences de l’Univers of the Centre National de la Recherche Scientifique of France, and the University of Hawaii. Mickaël Bonnefoy and Philippe Delorme acknowledge support in France from the French National Research Agency (ANR) through project grant ANR-20-CE31-0012 and the Programmes Nationaux de Planetologie et de Physique Stellaire (PNP and PNPS). B.L. acknowledges the support of Bobby Bus for the help and guidance on observing with IRTF SpeX. This research has benefited from the SpeX Prism Spectral Libraries, maintained by Adam Burgasser at <http://pono.ucsd.edu/~adam/browndwarfs/spexprism/>. This publication makes use of data products from the Wide-field Infrared Survey Explorer, which is a joint project of the University of California, Los Angeles, and the Jet Propulsion Laboratory/California Institute of Technology, funded by the National Aeronautics and Space Administration. This publication makes use of data products from the Two Micron All Sky Survey, which is a joint project of the University of Massachusetts and the Infrared Processing and Analysis Center/California Institute of Technology, funded by the National Aeronautics and Space Administration and the National Science Foundation. This publication makes use of

data products from the Wide-field Infrared Survey Explorer, which is a joint project of the University of California, Los Angeles, and the Jet Propulsion Laboratory/California Institute of Technology, funded by the National Aeronautics and Space Administration. This work has made use of data from the European Space Agency (ESA) mission Gaia (<https://www.cosmos.esa.int/gaia>), processed by the Gaia Data Processing and Analysis Consortium (DPAC, <https://www.cosmos.esa.int/web/gaia/dpac/consortium>). This research has made use of the services of the ESO Science Archive Facility. This research has made use of the SIMBAD database, operated at CDS, Strasbourg, France, and NASA’s Astrophysics Data System.

Software: *astropy* (Astropy Collaboration et al. 2013, 2018).

ORCID iDs

Bhavana Lalchand  <https://orcid.org/0000-0003-1618-2921>
 Wen-Ping Chen  <https://orcid.org/0000-0003-0262-272X>
 Beth A. Biller  <https://orcid.org/0000-0003-4614-7035>
 Sophie Dubber  <https://orcid.org/0000-0001-6951-469X>
 Zhoujian Zhang  <https://orcid.org/0000-0002-3726-4881>
 Michael C. Liu  <https://orcid.org/0000-0003-2232-7664>
 Jessy Jose  <https://orcid.org/0000-0003-4908-4404>
 Tanvi Sharma  <https://orcid.org/0000-0003-1634-3158>
 Mickaël Bonnefoy  <https://orcid.org/0000-0001-5579-5339>

References

- Allard, F., Hauschildt, P. H., Alexander, D. R., Tamanai, A., & Schweitzer, A. 2001, *ApJ*, 556, 357
- Allers, K. N., Jaffe, D. T., & Luhman, K. L. 2007, *ApJ*, 657, 511
- Allers, K. N., & Liu, M. C. 2013, *ApJ*, 772, 79
- Allers, K. N., & Liu, M. C. 2020, *PASP*, 132, 104401
- Alves de Oliveira, C., Moraux, E., Bouvier, J., et al. 2013, *A&A*, 549, A123
- Arce, H. G., Borkin, M. A., Goodman, A. A., Pineda, J. E., & Beaumont, C. N. 2011, *ApJ*, 742, 105
- Astropy Collaboration, Price-Whelan, A. M., Sipőcz, B. M., et al. 2018, *AJ*, 156, 123
- Astropy Collaboration, Robitaille, T. P., Tollerud, E. J., et al. 2013, *A&A*, 558, A33
- Bailer-Jones, C. A. L., Rybizki, J., Fousneau, M., Demleitner, M., & Andrae, R. 2021, *AJ*, 161, 147
- Bally, J., Devine, D., & Alten, V. 1996, *ApJ*, 473, 921
- Bally, J., Walawender, J., Johnstone, D., Kirk, H., & Goodman, A. 2008, in *Handbook of Star Forming Regions, Volume I: The Northern Sky*, ed. B. Reipurth, Vol. 4 (San Francisco, CA: ASP), 308
- Baraffe, I., Chabrier, G., Barman, T. S., Allard, F., & Hauschildt, P. H. 2003, *A&A*, 402, 701
- Baraffe, I., Homeier, D., Allard, F., & Chabrier, G. 2015, *A&A*, 577, A42
- Beichman, C. A., Jennings, R. E., Emerson, J. P., et al. 1984, *ApJL*, 278, L45
- Bell, C. P. M., Naylor, T., Mayne, N. J., Jeffries, R. D., & Littlefair, S. P. 2013, *MNRAS*, 434, 806
- Bensch, F. 2006, *A&A*, 448, 1043
- Bessell, M. S., & Brett, J. M. 1988, *PASP*, 100, 1134
- Bhatt, H. C. 1986, *MNRAS*, 222, 383
- Blanton, M. R., Bershady, M. A., Abolfathi, B., et al. 2017, *AJ*, 154, 28
- Burrows, A., Marley, M., Hubbard, W. B., et al. 1997, *ApJ*, 491, 856
- Cardelli, J. A., Clayton, G. C., & Mathis, J. S. 1989, *ApJ*, 345, 245
- Carpenter, J. M. 2001, *AJ*, 121, 2851
- Chambers, K. C., Magnier, E. A., Metcalfe, N., et al. 2016, arXiv:1612.05560
- Chen, W. P., Lee, H. T., & Sanchawala, K. 2007, in *Triggered Star Formation in a Turbulent ISM*, ed. B. G. Elmegreen & J. Palous, 237 (Cambridge: Cambridge Univ. Press), 278
- Chiang, P., Chen, W.-P., Albert, L., Liu, M., & Magnier, E. A. 2015, *MNRAS*, 448, 522
- Cieza, L., Williams, J., Kourkchi, E., et al. 2015, *MNRAS*, 454, 1909
- Cottaar, M., Covey, K. R., Meyer, M. R., et al. 2014, *ApJ*, 794, 125
- Cushing, M. C., Rayner, J. T., & Vacca, W. D. 2005, *ApJ*, 623, 1115

- Cutri, R. M., Skrutskie, M. F., van Dyk, S., et al. 2003, *VizieR Online Data Catalog*, **II/246**
- Cutri, R. M., Wright, E. L., Conrow, T., et al. 2012, *VizieR On-line Data Catalog*, **II/311**
- de Zeeuw, P. T., Hoogerwerf, R., de Bruijne, J. H. J., Brown, A. G. A., & Blaauw, A. 1999, *AJ*, **117**, 354
- Dickman, R. L. 1978, *ApJS*, **37**, 407
- Dubber, S., Biller, B., Allers, K., et al. 2021, *MNRAS*, **505**, 4215
- Dunham, M. M., Allen, L. E., Evans, N. J. I., et al. 2015, *ApJS*, **220**, 11
- Dunham, M. M., Crapsi, A., Evans, & Neal, J. 2008, *ApJS*, **179**, 249
- Dupuy, T. J., & Liu, M. C. 2017, *ApJS*, **231**, 15
- Epchtein, N., de Batz, B., Copet, E., et al. 1994, *Ap&SS*, **217**, 3
- Evans, N. J. I., Dunham, M. M., Jørgensen, J. K., et al. 2009, *ApJS*, **181**, 321
- Filippazzo, J. C., Rice, E. L., Faherty, J., et al. 2015, *ApJ*, **810**, 158
- Fitzpatrick, E. L. 1999, *PASP*, **111**, 63
- Forbes, J. C., & Loeb, A. 2019, *ApJ*, **871**, 227
- Fuller, G. A., Myers, P. C., Welch, W. J., et al. 1991, *ApJ*, **376**, 135
- Gaia Collaboration, Brown, A. G. A., Vallenari, A., et al. 2018, *A&A*, **616**, A1
- Gaia Collaboration, Brown, A. G. A., Vallenari, A., et al. 2021, *A&A*, **649**, A1
- Gaia Collaboration, Prusti, T., de Bruijne, J. H. J., et al. 2016, *A&A*, **595**, A1
- Goldsmith, P. F., Langer, W. D., & Wilson, R. W. 1986, *ApJL*, **303**, L11
- Hartmann, D., & Burton, W. B. 1997, *Atlas of Galactic Neutral Hydrogen* (Cambridge: Cambridge Univ. Press)
- Hatchell, J., Fuller, G. A., & Richer, J. S. 2007, *A&A*, **472**, 187
- Hatchell, J., Richer, J. S., Fuller, G. A., et al. 2005, *A&A*, **440**, 151
- Heiles, C. 1984, *ApJS*, **55**, 585
- Herbig, G. H., & Jones, B. F. 1983, *AJ*, **88**, 1040
- Herczeg, G. J., & Hillenbrand, L. A. 2014, *ApJ*, **786**, 97
- Herczeg, G. J., & Hillenbrand, L. A. 2015, *ApJ*, **808**, 23
- Hsieh, T.-H., & Lai, S.-P. 2013, *ApJS*, **205**, 5
- Jørgensen, J. K., Harvey, P. M., Evans, N. J. I., et al. 2006, *ApJ*, **645**, 1246
- Jose, J., Biller, B. A., Albert, L., et al. 2020, *ApJ*, **892**, 122
- Kirk, H., Johnstone, D., & Di Francesco, J. 2006, *ApJ*, **646**, 1009
- Kirkpatrick, J. D., Cushing, M. C., Gelino, C. R., et al. 2011, *ApJS*, **197**, 19
- Kirkpatrick, J. D., Looper, D. L., Burgasser, A. J., et al. 2010, *ApJS*, **190**, 100
- Knapp, G. R., Leggett, S. K., Fan, X., et al. 2004, *AJ*, **127**, 3553
- Koenig, X. P., & Leisawitz, D. T. 2014, *ApJ*, **791**, 131
- Langer, W. D., Velusamy, T., & Xie, T. 1996, *ApJL*, **468**, L41
- Langer, W. D., Wilson, R. W., Goldsmith, P. F., & Beichman, C. A. 1989, *ApJ*, **337**, 355
- Lawrence, A., Warren, S. J., Almaini, O., et al. 2007, *MNRAS*, **379**, 1599
- Lee, H.-T., & Chen, W. P. 2007, *ApJ*, **657**, 884
- Lee, H.-T., Chen, W. P., Zhang, Z.-W., & Hu, J.-Y. 2005, *ApJ*, **624**, 808
- Leggett, S. K., Currie, M. J., Varricatt, W. P., et al. 2006, *MNRAS*, **373**, 781
- Lucas, P. W., & Roche, P. F. 2000, *MNRAS*, **314**, 858
- Lucas, P. W., Roche, P. F., Allard, F., & Hauschildt, P. H. 2001, *MNRAS*, **326**, 695
- Luhman, K. L., Esplin, T. L., & Loutrel, N. P. 2016, *ApJ*, **827**, 52
- Luhman, K. L., Mamajek, E. E., Shukla, S. J., & Loutrel, N. P. 2017, *AJ*, **153**, 46
- Luhman, K. L., & Rieke, G. H. 1999, *ApJ*, **525**, 440
- Luhman, K. L., Stauffer, J. R., Muench, A. A., et al. 2003, *ApJ*, **593**, 1093
- McCray, R., & Kafatos, M. 1987, *ApJ*, **317**, 190
- McMahon, R. G., Banerji, M., Gonzalez, E., et al. 2013, *Msngr*, **154**, 35
- Meyer, M. R., Calvet, N., & Hillenbrand, L. A. 1997, *AJ*, **114**, 288
- Muench, A. A., Lada, C. J., Luhman, K. L., Muzerolle, J., & Young, E. 2007, *AJ*, **134**, 411
- Olmi, L., Testi, L., & Sargent, A. I. 2005, *A&A*, **431**, 253
- Ortiz-León, G. N., Loinard, L., Dzib, S. A., et al. 2018, *ApJ*, **865**, 73
- Pezzuto, S., Benedettini, M., Di Francesco, J., et al. 2021, *A&A*, **645**, A55
- Pineda, J. E., Offner, S. S. R., Parker, R. J., et al. 2015, *Natur*, **518**, 213
- Puget, P., Stadler, E., Doyon, R., et al. 2004, *Proc. SPIE*, **5492**, 978
- Rayner, J. T., Cushing, M. C., & Vacca, W. D. 2009, *ApJS*, **185**, 289
- Rayner, J. T., Toomey, D. W., Onaka, P. M., et al. 2003, *PASP*, **115**, 362
- Rebolo, R., Martin, E. L., Basri, G., Marcy, G. W., & Zapatero-Osorio, M. R. 1996, *ApJL*, **469**, L53
- Rebull, L. M., Stapelfeldt, K. R., Evans, N. J. I., et al. 2007, *ApJS*, **171**, 447
- Ridge, N. A., Di Francesco, J., Kirk, H., et al. 2006a, *AJ*, **131**, 2921
- Ridge, N. A., Schnee, S. L., Goodman, A. A., & Foster, J. B. 2006b, *ApJ*, **643**, 932
- Ruíz-Rodríguez, D., Cieza, L. A., Williams, J. P., et al. 2018, *MNRAS*, **478**, 3674
- Sancisi, R., Goss, W. M., Anderson, C., Johansson, L. E. B., & Winnberg, A. 1974, *A&A*, **35**, 445
- Schlafly, E. F., Green, G., Finkbeiner, D. P., et al. 2014, *ApJ*, **786**, 29
- Ridge, N. A., Di Francesco, J., Kirk, H., et al. 2006a, *AJ*, **131**, 1163
- Sumi, T., Kamiya, K., Bennett, D. P., et al. 2011, *Natur*, **473**, 349
- Tafalla, M., Kumar, M. S. N., & Bachiller, R. 2006, *A&A*, **456**, 179
- Trullols, E., & Jordi, C. 1997, *A&A*, **324**, 549
- Walawender, J., Bally, J., Francesco, J. D., Jørgensen, J., & Getman, K. 2008, in *Handbook of Star Forming Regions, Volume I: The Northern Sky*, ed. B. Reipurth, Vol. 4 (San Francisco, CA: ASP), **346**
- Walawender, J., Bally, J., & Reipurth, B. 2005, *AJ*, **129**, 2308
- Wright, E. L., Eisenhardt, P. R. M., Mainzer, A. K., et al. 2010, *AJ*, **140**, 1868
- Yao, Y., Meyer, M. R., Covey, K. R., Tan, J. C., & Da Rio, N. 2018, *ApJ*, **869**, 72
- Young, K. E., Young, C. H., Lai, S.-P., Dunham, M. M., & Evans, N. J. I. 2015, *AJ*, **150**, 40
- Yu, K. C., Billawala, Y., & Bally, J. 1999, *AJ*, **118**, 2940
- Zapata, L. A., Arce, H. G., Brassfield, E., et al. 2014, *MNRAS*, **441**, 3696
- Zari, E., Hashemi, H., Brown, A. G. A., Jardine, K., & de Zeeuw, P. T. 2018, *A&A*, **620**, A172
- Zavagno, A., Deharveng, L., Comerón, F., et al. 2006, *A&A*, **446**, 171
- Zhang, Z., Liu, M. C., Best, W. M. J., et al. 2018, *ApJ*, **858**, 41
- Zucker, C., Schlafly, E. F., Speagle, J. S., et al. 2018, *ApJ*, **869**, 83